RSC Advances

ROYAL SOCIETY OF CHEMISTRY

www.rsc.org/advances

Synthesis of colloidal MnO_2 with sheet-like structure by one-pot plasma discharge in permanganate aqueous solution

Hyemin Kim [a], Anyarat Watthanaphanit [a,b], and Nagahiro Saito [a,b,c,*]

[a] *Graduate School of Engineering, Nagoya University, Furo-cho, Chikusa-ku, Nagoya 464-8603, Japan*

[b] *Social Innovation Design Center, Institute of Innovation for Future Society, Nagoya University, Furo-cho, Chikusa-ku, Nagoya 464-8603, Japan*

[c] *Green Mobility Collaborative Research Center, Nagoya University, Furo-cho, Chikusa-ku, Nagoya 464-8603, Japan*

GRAPHICAL ABSTRACT

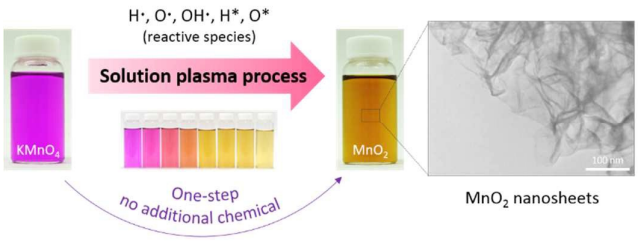

ABSTRACT

Stable colloidal MnO_2—consisting of MnO_2 with sheet-like structure—was synthesized by solution plasma process (SPP). The synthesis was completed within one-step by discharging the plasma in potassium permanganate ($KMnO_4$) aqueous solution without utilizing any dispersants or stabilizers. An alteration of the manganese oxide oxidation states, from MnO_4^- to MnO_2 as a function of the discharge time, was investigated by UV-vis spectroscopy. Morphology and elemental constituent were observed by TEM and EDS mapping. Results indicated that the discharge time was an important feature for the formation of MnO_2 in the SPP system. Specifically at the neutral pH (pH = 7), MnO_4^- was completely reduced to MnO_2 within a discharge time of 18 min. After that the obtained MnO_2 was converted rapidly to Mn^{2+}. To better understand the possible pathways of the MnO_2 formation by the SPP, we compared the aspect of reaction at different pH conditions. Formation of MnO_2 at additional controlled pH, *i.e.* 2 and 12, was studied. Results suggested that hydrogen

species played a key role for the reduction of MnO_4^- in the water-based SPP system. Comparison to the existing routes for the synthesis of MnO_2 nanosheets with single or a low number of layers, the SPP hold excellent promise as an effective alternative means regarding its simplicity, time-energy preserving, and scalability.

Keywords: Colloid, Manganese dioxide (MnO_2), Sheet-like structure, Solution plasma process (SPP)

1. Introduction

Nanostructured manganese dioxide (MnO_2) have been paid particular attention in scientific and materials engineering fields due to its excellent electrochemical properties which lead to extensive applications in various fields (*i.e.*, electrode material for Li-battery and supercapacitor, environmental remediation, oxidative degradation, catalyst, biosensor, magnetic material, and ion-exchanger) as well as its low cost, earth-abundant, and eco-friendliness [1–2]. It is known that MnO_2 has several type of crystallographic structures and morphologies which are different in the ways that its basic structural unit [MnO_6] octahedron are linked. Based on the different [MnO_6] links, MnO_2 can be divided into the chain-like tunnel-type (1D: *i.e.*, α-, β-, and γ-MnO_2), the sheet/layered-type (2D: *i.e.*, δ-MnO_2), and the spinel-type (3D: *i.e.*, λ-type) [3–6]. It is obviously that performance of the MnO_2, such as capacitance, cycling stability, catalytic activity, is highly dependent on its crystallographic forms and morphologies. Among them, layered-type MnO_2 (birnessite or δ-MnO_2) has been attracted sustained interest over the last several decades due to its unique structural properties. It is able to degrade organic pollutants and fix trace-metal elements which is thus powerful for the removal of contaminants in environments [7]. Besides, the birnessite MnO_2 exhibits higher area-normalized capacitance values compared with the tunnel type [8–9], owing to its layered structure consisting of cations (*e.g.*, K^+, Li^+, Na^+, *etc*.) and water (H_2O) inserting in its interlayer spaces [9–10]. Its sufficient interlayer distance consequently allows large ions to be diffused through effectively. In comparison, while the interlayer distance of the birnessite MnO_2 is ~7 Å, tunnel size of the 1D tunnel MnO_2 is quite narrow (*i.e.*, β-MnO_2: ~1.89 Å, γ-MnO_2: ~1.89 and ~2.3 Å). These narrow tunnels prohibit the intercalation of cations as well as other molecules. As a result, specific capacitance of MnO_2 with different crystallographic structures generally follows the order: $\alpha \simeq \delta > \gamma > \lambda > \beta$ [11].

Various synthesis methods have therefore been searched to acquire the layered-type MnO_2,

especially, nanosheets with single or a low number of layers [12]. Notwithstanding that the synthesis is generally performed via multi-step process and with the assistance of mechanical or chemical treatments where complex type of reactor is required. For example, Sun *et al.* [13] started the synthesis from preparing δ-phase MnO_2 through a microwave-assistant hydrothermal process by heating a mixture of $KMnO_4$ powder and hydrochloric acid (HCl) aqueous solution (at 150 °C) in a sealed reactor with controlled microwave radiation in a commercial CEM Discover system. Black powder consisting of flower-like morphology of the MnO_2 multilayer nanosheets was obtained from this step. Then single-layer MnO_2 nanosheets were acquired by mechanically compressing the as-prepared MnO_2 powder in a diamond anvil cell. Apart from this technique, MnO_2 multilayer nanosheets could be separated to a single 2D nanosheet by swelling and exfoliation, using surfactant (*e.g.*, tetrabutylammonium hydroxide) [14] or be produced with the aid of template such as graphene oxide [15]. Accordingly, exploration of a fast, facile, scalable, and efficient time-energy consuming synthetic methods remains a challenge.

Recently, pulsed plasma in liquid phase named "solution plasma process (SPP)" has attracted much interest as a promising method for the synthesis of nanomaterial [16], the depolymerization of biopolymer [17], the production of carbon material for utilizing as electrode of Li-air battery and fuel cell [18], and the water treatment [19]. It superiors are simple experimental apparatus, short processing time (in the range of within several minutes), processing condition at room temperature and atmospheric pressure, and minimization of chemical reagents [20–21]. It also has a potential for the mass production by using multiple electrodes and flow system. For nanomaterial synthesis, the main reaction occurring in the SPP system is redox reaction driven by reactive species such as radicals, electrons, and ions generated by plasma in the liquid media that can lead to the reduction of ions to nanomaterials [22].

In this study, we applied the SPP for one-pot synthesis of nanostructured MnO_2 to overcome the above mentioned limitations of the existing methods. We simply synthesized stable colloidal MnO_2 with sheet-like structure by discharging the plasma in $KMnO_4$ aqueous solution within several minutes and without the addition of any regents. MnO_2 formation was verified by UV-vis and Raman spectroscopy while morphology of the MnO_2 disseminated in the colloids was characterized by TEM, XRD, XPS and EDS elemental mapping. Possible reduction mechanisms for the alteration of MnO_4^- to MnO_2 by the plasma discharge in $KMnO_4$ aqueous solution was also investigated by carrying out experiment at additional pH

conditions, *i.e.*, at pH = 2 and 12; representing a hydrogen-rich (H-rich) and hydrogen-poor (H-poor) conditions, respectively. Results are discussed in the final section of this paper.

2. Experimental section

2.1. Chemicals

Potassium permanganate ($KMnO_4$, > 99.3%) purchased from Wako Pure Chemical Industries Ltd. (Osaka, Japan) was used as a manganese dioxide precursor. Sulfuric acid (H_2SO_4, 96.0%) and sodium hydroxide solution (NaOH, 48.0%) purchased from Kanto Chemical Co., Inc. (Tokyo, Japan) were used for pH adjustment. All potassium permanganate aqueous solutions were prepared using ultrapure water (resistivity = 18.2 MΩ·cm at 25 °C) obtained from Aquarius water distillation apparatus, RFD250NB, Advantec (Tokyo, Japan).

2.2. Experimental setup and sample preparation

Fig. 1 shows schematic illustration of the SPP system used for synthesizing colloidal MnO_2 in this study. Possible interfaces appearing in the system are additionally illustrated. A pair of 1 mm diameter tungsten rods (purity 99.9%, Nilaco Corp., Japan) was used as electrodes. Each of them was covered with ceramic tube before inserted into silicone plug and placed in the middle part of a glass reactor. Distance between two electrode tips was controlled to be 0.5 mm. Before the plasma discharge, 100 mL of 0.2 mM $KMnO_4$ aqueous solution was put in the glass reactor. The plasma was generated by using a bipolar-DC pulsed power supply (Kurita, Japan) while the pulse width and frequency were fixed at 1.5 μs and 20 kHz, respectively. The reaction was operated at atmospheric pressure and room temperature, and solution was stirred continuously during the operation in order to maintain an equivalent reaction at any instant.

In order to find information about the presence of radicals and other reactive species produced in the system, optical emission spectrum was taken by using optical emission spectroscope (Ocean Optics USB2000+, Ocean Optics Inc., USA) during the plasma generation. The spectrum was collected in the spectral region from 300 to 1000 nm with an integration time of 200 ms and average 10 scans. To verify the possible reaction mechanism, effect of the pH condition on the formation of the colloidal MnO_2 was investigated. The pH of solutions was adjusted by dropping the as-received H_2SO_4 (96.0%) or NaOH (48.0%) slowly into the 0.2 mM $KMnO_4$ aqueous solution to attain the desired pH of 2 and 12. The pH measurement was performed using pH/ion meter (F-53, Horiba, Japan).

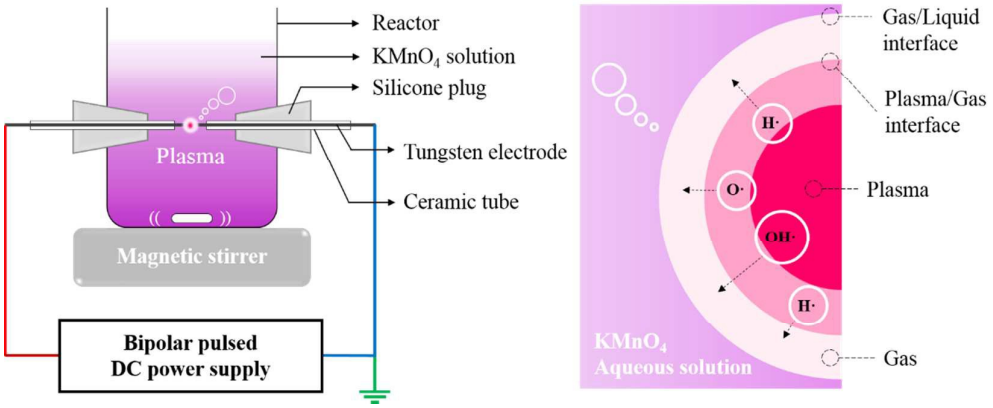

Fig. 1 Schematic illustration of solution plasma process (SPP) experimental setup, along with possible interfaces appearing in the system.

2.3. Characterizations

An alteration of the manganese oxide oxidation states, from MnO_4^- to MnO_2 as a function of the discharge time, was monitored by UV-vis spectrophotometer (Shimadzu UV-3600, Japan). The spectra were collected in the spectral range from 250 to 700 nm. The Tyndall effect test was done in order to confirm an incident of the colloidal formation by directing a laser beam through a solution. Photograph of the solution was then taken. Stability of the synthesized colloidal MnO_2 was determined, after the suspension was stored at room temperature up to six months, using a zeta potential analyzer (ELS-7300K, Photal Otsuka Electronics, Japan). To investigate morphology and elemental constituent of the synthesized samples, transmission electron microscopy (TEM) and energy dispersive spectroscopy (EDS) elemental mapping images were collected with JEM-2500SE (JEOL, Japan) operated at an acceleration voltage of 200 kV. TEM sample was prepared by dropping the colloidal MnO_2 solution onto amorphous carbon-coated copper grids without any additional treatment before air drying. X-ray diffraction (XRD) pattern was collected, to elucidate the MnO_2 crystalline structure, using a Rigaku SmartLab with Cu K_α (λ = 1.5418 Å) radiation, operating at 40 kV and 30 mA (1.2 kW). The XRD sample was prepared by the drop casting method, *i.e.*, the colloidal MnO_2 was dropped onto a quartz substrate (zero-background holder) before drying at room temperature until the film was formed. X-ray photoelectron spectroscopy (XPS) analysis was carried out on PHI 5000 VersaProbe II with monochromated Al Kα radiation. The MnO_2 structural property was additionally confirmed by Raman spectroscopy. A small

amount of MnO_2 powder was separated from the colloidal suspension by centrifugation for Raman testing. Raman spectrum was recorded on an Olympus BX51RF Raman spectrometer (Tokyo, Japan).

3. Results and discussion

3.1. Synthesis of colloidal MnO_2

We found that the reduction of MnO_4^- to other oxidation states of manganese oxide in pure water without any treatment was not feasible. In this study, colloidal MnO_2 was synthesized by discharging plasma in $KMnO_4$ aqueous solution. Change of the solution color along with the MnO_2 formation were investigated every 2 min interval. The latter result was confirmed by ultraviolet-visible spectroscopy (UV-vis). Fig. 2a shows UV-vis adsorption spectra of $KMnO_4$ aqueous solution (pH = 7) before and after the plasma generation. The absorption peaks in the range of 500–570 nm which exhibited maximum absorption wavelengths (λ_{max}) at 507, 525, 545 and 569 nm were characteristic peaks of MnO_4^-. After the plasma was generated, peaks of MnO_4^- gradually disappeared while a new absorption peak with a λ_{max} covering the range of 350–360 nm—an assignment of MnO_2 nanostructure—was evidenced [23–24]. As can be seen from Fig. 2a, MnO_2 peaks become more perspicuous with an increment of peak intensity when the plasma discharge time was extended. To clearer notify the peak intensity change, plots of absorbance at 545 nm and 356 nm versus times are indicated in Fig. 2b. The sharp decline of peaks at 545 nm and the increment of peaks at 356 nm specified the conversion of MnO_4^- to MnO_2. Among the observed time intervals, the absorption peak with the greatest intensity was observed at 18 min. The alteration of solution colors during this range of observation is shown in Fig. 2c. Clearly, color of the solution changed from purple to red purple and finally brown when the discharge time was prolonged. Particularly, the brown color is a characteristic of the colloidal MnO_2.

On the other hand, characteristic peak of MnO_2 (λ_{max} = 356 nm) gradually decreased when the discharge time was greater than 18 min (Fig. 2d and 2e). Furthermore, the reduction time of peaks was faster than that was observed for the conversion of MnO_4^- to MnO_2. During this range of discharge times (*i.e.*, 19–23 min), solution colors were changed from brown to light yellow (Fig. 2f) indicating the deterioration of MnO_2 to Mn^{2+}. Depending on their oxidation states, manganese ions have various colors. Particularly, Mn(VII)-corresponds to MnO_4^-; Mn(IV)-corresponds to MnO_2; and Mn(II)-corresponds to Mn^{2+}, exhibit purple, brown, and light yellow (or colorless), respectively [25]. Therefore, the reduction of MnO_4^- to other

oxidation states can be presumed by the solution color change. The aforementioned results suggested that the discharge time was an important feature for the formation of MnO_2 in the SPP system.

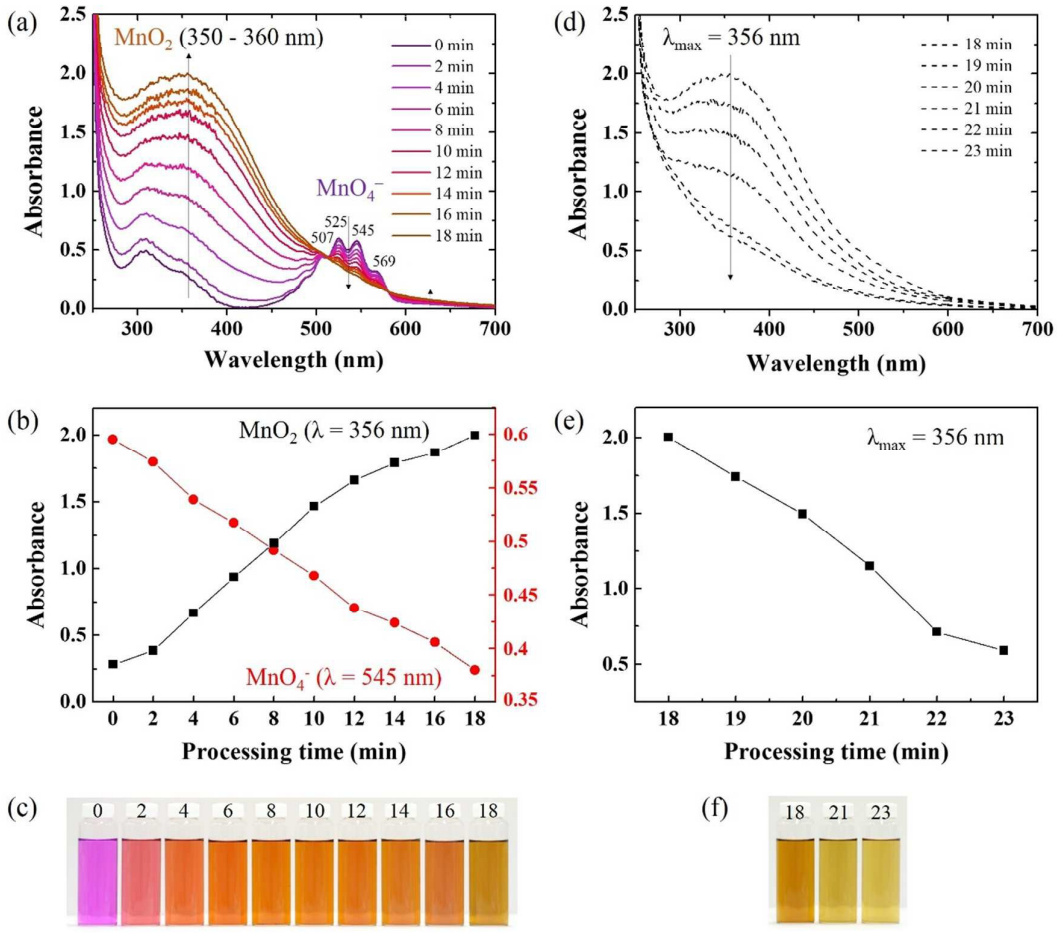

Fig. 2 (a) UV-vis absorption spectra of the SPP treated $KMnO_4$ aqueous solutions with discharge times of 0–18 min, along with (b) the time-absorbance plots of MnO_2 (■, λ = 356 nm) and MnO_4^- (●, λ = 545 nm), and (c) photographs of the obtained solutions as a function of discharge time. (d) UV-vis absorption spectra of the solution during the discharge times of 18–23 min, along with (e) the time-absorbance plots (■, λ = 356 nm), and (f) photographs of the obtained solutions.

3.2. Colloidal property and stability of the colloidal MnO_2

Colloidal property of the synthesized MnO_2 was confirmed by testing for the Tyndall

phenomenon. Briefly, when a strong beam of light is pass through a colloidal solution, the light is scattered by the colloidal particles. This scattering of light is called "*Tyndall effect*". As can be clearly seen from Fig. 3a, the observed light scattered line in the SPP discharged sample confirmed the colloidal MnO_2 formation. Additionally, comparison test was performed by directing the beam through three solution samples, *i.e.*, deionized (D. I.) water, $KMnO_4$ aqueous solution, and colloidal MnO_2 simultaneously. It was obviously that the Tyndall effect occurred only in the colloidal MnO_2 sample (Fig. 3b).

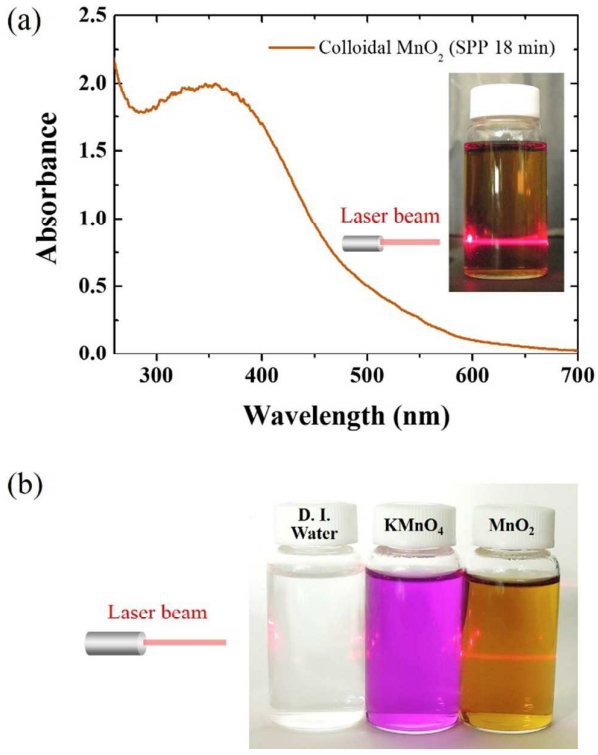

Fig. 3 (a) UV-vis absorption spectrum of colloidal MnO_2 synthesized at the SPP processing time of 18 min, along with photographs of the solution when a laser beam was directed through (a) colloidal MnO_2 solution and (b) solutions with the following order: deionized (D. I.) water, $KMnO_4$ aqueous solution, and colloidal MnO_2.

To determine stability of the colloidal MnO_2, zeta-potential measurement was carried out after the sample was left standing at room temperature for six months. Zeta-potential is a term for determining stability of a colloidal system. Generally, dividing position between stable and unstable state of a colloidal suspension is ± 30 mV. The aggregation of particles is

less at the optimal zeta-potential (*i.e.*, > +30 or < –30 mV) due to electrostatic repulsion among the colloidal particles [26–27]. From our observation, average zeta-potential of the synthesized colloidal MnO_2 was found to be –33.8 ± 1.27 mV, indicating a relatively good stability. As a consequence, precipitation of the suspension was not observed although six months have passed.

3.3. Characterization of morphology and chemical composition

Fig. 4 shows TEM images of the MnO_2 disseminated in the synthesized colloids. The as-prepared MnO_2 exhibited sheet-like structures where some sections were folding. Like another 2D material: graphene; folding of the sheet could occur due to its high surface tension [28]. Aggregated lamellar structure with size of several hundred nanometers (~100–300 nm) was also observed in some parts. Note that this morphology was found in overall area of the observed sample. XRD spectrum along with its indexed pattern are shown in Fig.5. The broad and low intensity of the XRD peaks could be caused by the limitation of sample preparation for characterization, *i.e.*, very thin film could be formed and thus included only small amount of particles. By matching with the XRD indexing software, the diffraction peaks corresponded to a potassium birnessite-MnO_2 (JCPDS No. 01-080-1098, monoclinic, C2/m, a = 5.15 Å, b = 2.84 Å, c = 7.17 Å).

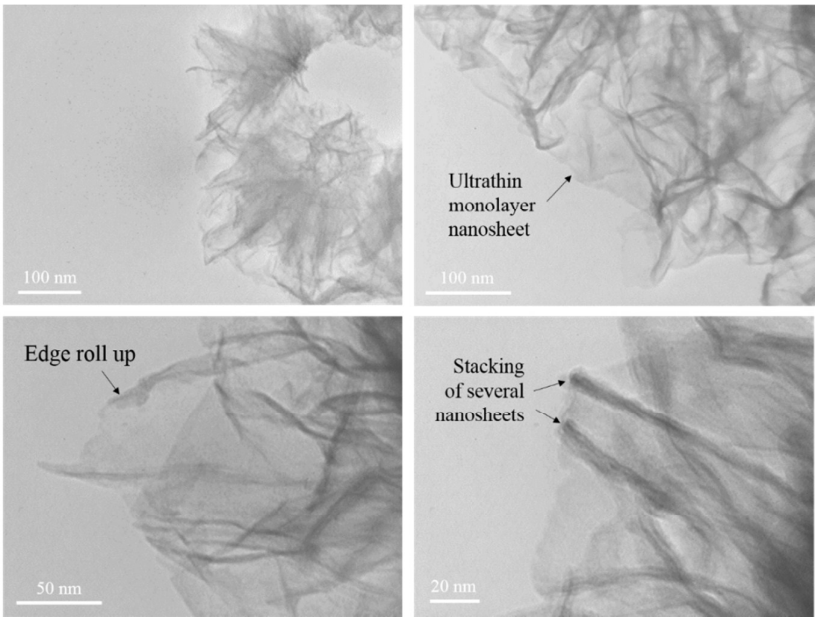

Fig. 4 Selected TEM images of the MnO_2 disseminated in the synthesized colloids.

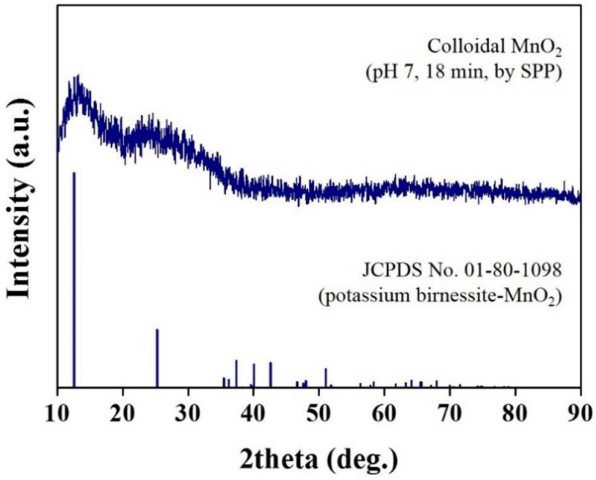

Fig. 5 XRD pattern of the as-prepared MnO_2, along with its indexed pattern.

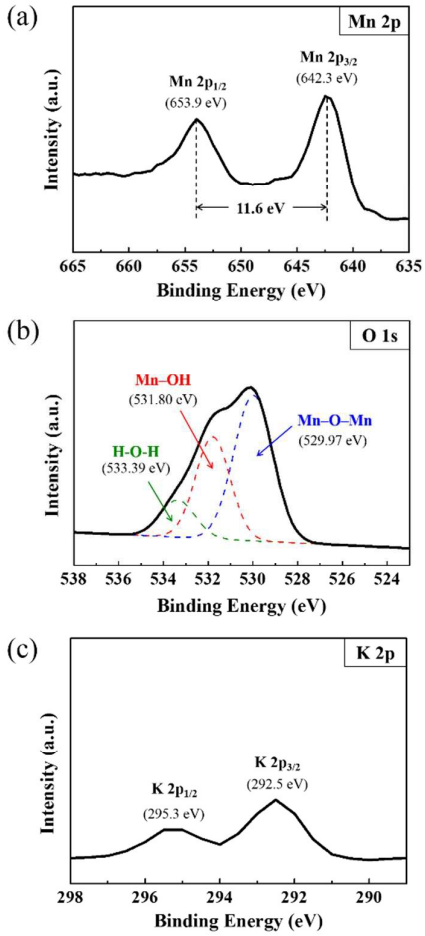

Fig. 6 XPS spectra of the as-synthesized MnO_2 (a) Mn 2p, (b) O 1s and (c) K 2p.

More detailed information on the chemical composition and bonding state were additionally investigated by XPS, EDS elemental mapping and Raman spectroscopy. Fig. 6 shows XPS spectra of the as-prepared colloidal MnO_2 sample. The Mn 2p region (Fig. 6 (a)) indicated the peaks of Mn $2p_{3/2}$ and Mn $2p_{1/2}$ at 642.3 eV and 653.9 eV, respectively. The separation of energy by 11.6 eV represented the formation of MnO_2 with an oxidation state of +4 [15, 29, 30]. The O 1s spectrum (Fig. 6 (b)) was analyzed by curves fitting using Gaussian function and multi-peaks assignment. It was fitted with three peaks corresponding to Mn–O–Mn bond (529.97 eV), Mn–OH bond (531.80 eV), and H–O–H bond (533.39 eV) for the tetravalent oxide, hydroxide and water molecules, respectively [31–32]. In addition, the K 2p was measured. As shown in Fig. 6 (c), the broad two peaks at 292.5 eV and 295.3 eV indicated the K $2p_{3/2}$ and K $2p_{1/2}$, respectively. This corresponded to the presence of K in the lattice of MnO_2. The EDS images shown as Fig. 7 clearly indicated that the as-prepared sample was composed of manganese (Mn), oxygen (O) and potassium (K). An existence of K element in the sheet suggested that the synthesized MnO_2 was a birnessite type which K ions were intercalated between the MnO_2 layers. Structural feature of the synthesized MnO_2 of the birnessite family was additionally confirmed by Raman spectroscopy shown as supplementary information (see Fig. S1). Generally, characteristics of the birnessite-type MnO_2 are represented by three major Raman bands at 500–510, 575–585 and 625–650 cm^{-1}. From our result, the three mentioned bands were observed. Raman band at around 630 cm^{-1} can be recognized as the symmetric stretching vibration of Mn–O in the MnO_6 groups. Note that the band located below 560 cm^{-1} is usually attributed to the Mn–O stretching vibration in the basal plane of MnO_6 sheet [33–34]. Results indicated that the obtained products were birnessite-type MnO_2.

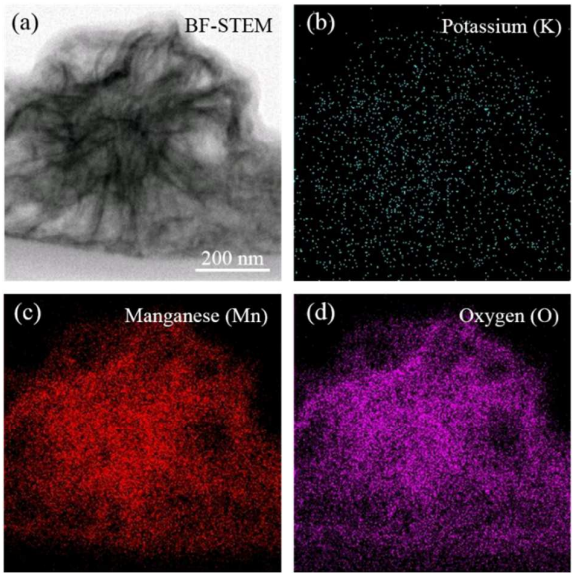

Fig. 7 (a) Bright field scanning TEM image and (b–d) EDS elemental mapping images of the MnO_2 taken from the respective area of the TEM, showing the distribution of (b) potassium, (c) manganese, and (d) oxygen.

Comparison to the existing routes for the synthesis of MnO_2 nanosheets with single or a low number of layers, the impact of the present strategy is remarkable. As mentioned in the introduction section that for the existing routes; dispersants, surfactants, or physical treatments (*e.g.*, microwave-assisted method, ultrasonication) are required as additional reagents and/or steps [14, 35]. On the other hand, we could simply produce MnO_2 nanosheets with mono or few layers in one step, in an uncomplicated reactor, at room temperature and atmospheric pressure, and without any chemicals; within several minutes. Through these results, it was confirmed prospectively that the method shown in the present contribution was effective for synthesizing mono- and few-layer MnO_2 nanosheets compared with the existing methods. However, formation mechanism of the MnO_2 nanosheets by the SPP is not clear yet. Thus, it is necessary to provide the exact guidelines for controlling the properties (*e.g.*, size and morphology) of the required MnO_2 through additional research at various SPP conditions.

3.4. Reactive species generated during MnO_2 formation

Normally, the SPP involves many physical and chemical reactions. When the high voltage and current source are applied through two submerged electrodes in an aqueous solution,

hydrogen and oxygen gas bubbles are generated rapidly. After that, electrical breakdown occurs. Owing to the growth of small bubbles, composing of water vapor and few electrons, plasma channel is formed [36]. Consequently, water molecules are dissociated by ions, electrons, and activated radicals in the plasma zone. To confirm the formation of reactive species during the plasma discharge in $KMnO_4$ aqueous solution (0.2 mM), optical emission spectroscopy (OES) measurement was carried out. OES spectrum is shown in Fig. 8. Clearly, emission peaks of hydrogen (H_α, λ = 656 nm; H_β, λ = 486 nm; H_γ, λ = 434 nm) and oxygen (O I, λ = 777 and 845 nm) species were observed. It is supposed that reduction reaction of MnO_4^- to MnO_2 could result from the reaction of the MnO_4^- precursor with hydrogen species since the eventual gain of electrons results in the decrease in the positive charge of Mn ions. To verify this assumption, experiments were conducted at additional pH conditions, *i.e.*, at pH = 2 and 12.

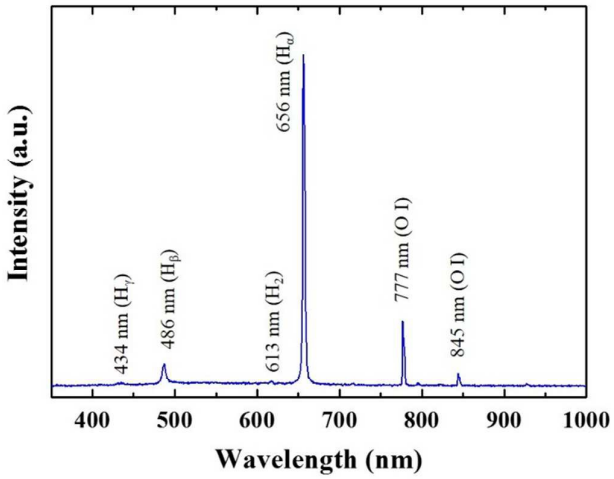

Fig. 8 OES spectrum of the plasma generated in 0.2 mM $KMnO_4$ aqueous solution.

3.5. Possible pathway of the MnO_2 formation by the SPP

To better understand the pathway of the MnO_2 formation by the SPP, we conducted the plasma discharge in $KMnO_4$ aqueous solution at additional pH conditions, *i.e.*, at pH = 2 and 12; representing a H-rich and a H-poor conditions, respectively. Then, optical absorption characteristics of the solutions were analyzed. UV-vis absorption spectra of the as-prepared solutions synthesized from different pH conditions are shown in Fig. 9. It was clearly seen that reduction reaction of MnO_4^- occurring at pH 2 (Fig. 9a) was faster than that of occurring at pH 7 (Fig. 9b), *i.e.*, peaks of MnO_4^- (~500–570 nm) disappeared after the reaction time of

only 6–7 min. However, characteristic absorption peaks of MnO_2 (λ_{max} ~300–400 nm) were not observed. The change in the solution color of pH 2 condition showed similar trend to that of at pH 7, *i.e.*, the solution color altered from purple to brown and then yellow (see Fig. S2). Considering the spectra of pH 12 condition (Fig. 9c), peak of MnO_2 was observed but at a longer reaction time compared with that of at pH 7. Specifically, while the highest peak intensity was observed at 18 min for pH 7; that of pH 12 was observed at 24 min. Furthermore, the solution color change was different from that of observed at pH 2 and 7, *i.e.*, the color changed from purple to dark purple before turning to brown (see Fig. S3). These findings suggested that hydrogen species were crucial for the reduction of MnO_4^- to MnO_2.

In order to confirm that an alteration of the absorption peaks as well as solution color were not due to the inclusion of acid or base in the system, the change in the UV-vis peak as well as the solution color of the untreated- pH 2 and pH 12 $KMnO_4$ aqueous solutions after one day of sample preparation were observed. Unchanging of the solution color and UV-vis peaks (see Fig. S4) certified that this effect was negligible.

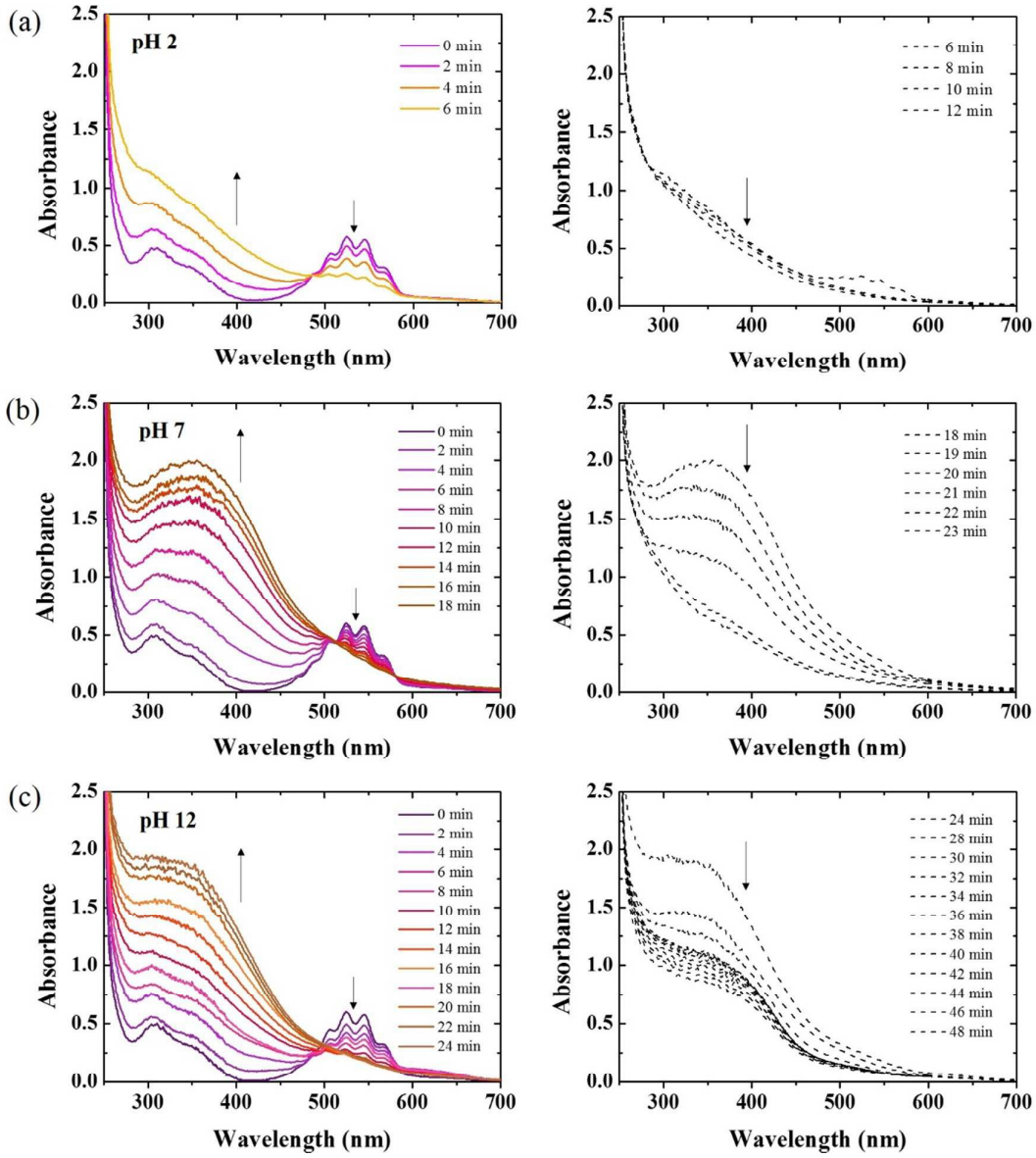

Fig. 9 UV-vis absorption spectra of the SPP treated $KMnO_4$ aqueous solutions with different pH conditions: (a) 2 (b) 7, and (c) 12.

We accordingly assumed possible reduction mechanisms of MnO_4^- to MnO_2 in the SPP system. Firstly, possible reactions occurring during the discharge at pH 7 were proposed. As can be seen from OES result (Fig. 7), when the plasma was generated in water-based solutions, highly reactive species such as H, O and OH occurred by water dissociation. Equations (1)–(2) indicate possible primary chemical reactions in the plasma zone.

$H_2O \rightarrow H\cdot + OH\cdot$ (1)

$2H_2O \rightarrow 2H_2 + O_2$ (2)

Besides, the produced reactive radicals could recombine each other and form H_2, O_2, as well as H_2O_2 as indicated in Equations (3)–(5) [37–38]. Although H_2O_2 was reported to have an effect on the reduction of MnO_4^- to MnO_2, *e.g.*, in sonochemical treatment [39], H radical was revealed to act as the major reductant in the SPP. Particularly, synthesis of gold nanoparticles by the SPP from gold precursor aqueous solution containing a spin trap agent—PBN (n-tert-buthyl-α-phenylnitrone), brought out this information [16].

$2H\cdot \rightarrow H_2$ (3)

$2O\cdot \rightarrow O_2$ (4)

$H_2 + O_2 \rightarrow H_2O_2$ (5)

Regarding the pH measurement before and after the plasma discharge, pH of the solution was found to increase from ~7 to ~9. It should therefore be postulated that hydroxyl ions (OH^-) were formed. Accordingly, we proposed Equations (6) to indicate possible reduction mechanism of MnO_4^- to MnO_2 in the SPP system.

$MnO_4^- + 3H\cdot \rightarrow MnO_2 + OH^- + H_2O$ (6)

In addition, when the discharge was continued after the optimal time, continuous reduction reaction of MnO_2 to Mn^{2+} might occur through the following equation:

$MnO_2 + 2H\cdot \rightarrow Mn^{2+} + 2OH^-$ (7)

Fig. 10 shows the conversion of the peak absorbance at 356 nm (MnO_2 characteristic peak) as a function of discharge time at different pH conditions. This result indicated the distinction in the rate of reduction from MnO_4^- to MnO_2 and from MnO_2 to Mn^{2+} at different pH conditions. It was observed that the rate of reduction from MnO_2 to Mn^{2+} was faster than that of from MnO_4^- to MnO_2 about 2–4 times. Considering effect of the solution pH, reduction rate at the H-rich conditions (pH = 2) was faster than that of at the control pH (pH = 7). Here,

while peaks of MnO_4^- disappeared after the plasma discharge, peak of MnO_2 was not observed (see also Fig. 9a). We supposed that owing to the rich of H species at the pH 2 condition, MnO_4^- was reduced directly to Mn^{2+} before MnO_2 was formed. On the other hand, at the H-poor condition (pH = 12), the reduction rate from MnO_4^- to MnO_2 and MnO_2 to Mn^{2+} was confirmed to be relatively slower. These results supported that H species played a key role in the reduction of MnO_4^- to MnO_2 in our system.

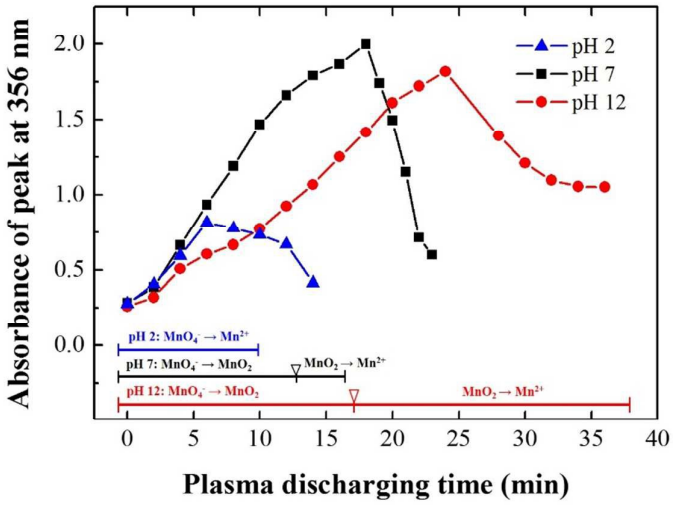

Fig. 10 Conversion of the peak absorbance at 356 nm (MnO_2 characteristic peak) as a function of discharge time at different pH conditions.

Based on the above results, possible formation mechanism of MnO_2 by discharging plasma in $KMnO_4$ aqueous solution was proposed, as shown in Fig. 11. We supposed that the pathway of reaction includes two main steps. Firstly, highly reactive species, especially hydrogen radicals, generated by the plasma discharge lead to the reduction of MnO_4^- ions and subsequently form MnO_6 octahedral unit ([MnO_6] octahedron). Secondly, for energy stabilization, each [MnO_6] octahedron shares two adjacent edges with its neighbors to form edge-sharing octahedral layers [15, 29] where the cations (*i.e.,* K^+ ions) and water molecules are occupied in the interlayer region, simultaneously.

However, we still do not know how the [MnO_6] octahedra link each other for the certain structure. According to previous reported study [29], various MnO_2 nanostructures with different morphologies could be affected by concentration and pH of the precursors as well as

the experimental conditions. Effect of the pH on morphology and colloidal stability of the synthesized MnO_2 was also found in our study. TEM images of the colloidal MnO_2 synthesized at pH 2, 7 and 12 are shown in Fig. S5. Clearly, sheet-like structures were observed in all conditions, but, with aggregated, stacked, or thicker forms for pH 2 and 12. As a consequence, stability of the colloidal MnO_2 synthesized at these conditions was lower than that of synthesized at pH 7. Tendency of the colloidal stability was in the following order: pH 7 > pH 2 > pH 12 (see Fig. S6 (a) Zeta potential values). These tendency was in accordance with photographs of samples after left standing for 3 months (Fig. S6 (b)), *i.e.*, while colloidal MnO_2 synthesized at pH 7 still dispersed well in the bottle, the colloids synthesized at pH 2 and 12 formed aggregates and precipitated. We believe that the exact synthetic guidelines for controlling the properties of the required MnO_2 (*e.g.,* morphology, structure, electrochemical property *etc.*) can be investigated through additional research at various precursors and SPP conditions.

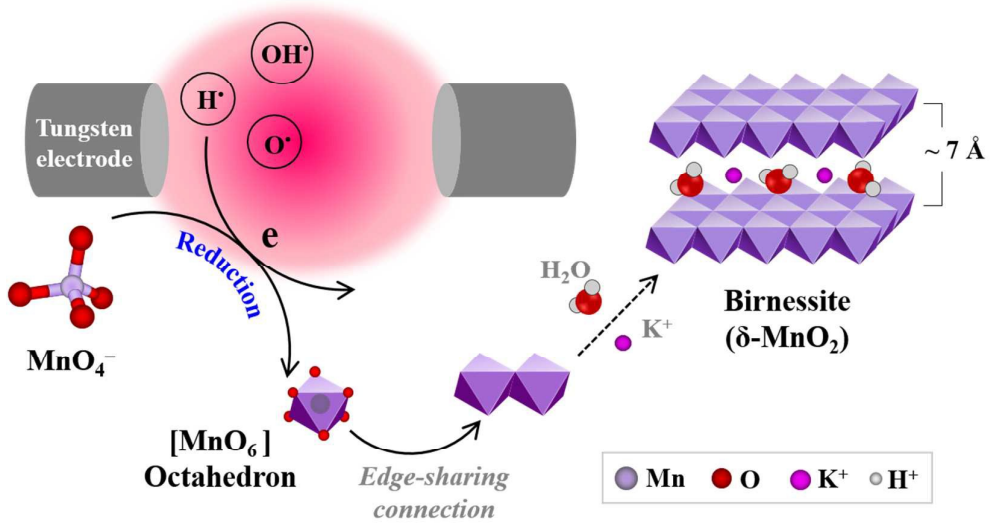

Fig. 11 Schematic illustration of the possible formation mechanism of MnO_2 by discharging plasma in $KMnO_4$ aqueous solution.

4. Conclusion

In this work, stable colloidal MnO_2 consisting of sheet-like structure with single or a low number of the MnO_2 sheet layers was simply synthesized by an alternative means—discharging plasma in an aqueous solution of $KMnO_4$ precursor—in one pot and without

utilizing any dispersants or stabilizers. The obtained MnO_2 nanosheet was confirmed to be a birnessite-type which K ions were intercalated between the MnO_2 layers. Additionally, the as-prepared samples displayed a long term dispersion stability for more than 6 months. Based on the results of carrying out the synthesis at different pH conditions, it should be confirmed that hydrogen species played a key role in the reduction of MnO_4^- to MnO_2. An alteration of the manganese oxide oxidation states was also remarkably influenced by the plasma discharge time. Regarding its simplicity and effectiveness, we are continuing our research on utilizing the SPP for further development on the synthesis of MnO_2 nanomaterials and investigating its potential as parts of energy-storage devices.

Acknowledgements

We greatly appreciate the financial support from the Core Research for Evolutional Science and Technology (CREST) of Japan Science and Technology (JST) Agency.

Notes and references

1 W. Wei, X. Cui, W. Chen and D. G. Ivey, *Chem. Soc. Rev.,* 2011, **40**, 1697–1721.

2 P. Simon and Y. Gogotsi, *Nature Mater.*, 2008, **7**, 845–854.

3 T. T. Truong, Y. Liu, Y. Ren , L. Trahey and Y. Sun, *ACS Nano*., 2012, **6**, 8067–8077.

4 F. Shi, L. Li, X. L. Wang, C. D. Gua and J. P. Tu, *RSC Adv*., 2014, **4**, 41910–41921.

5 K. Chen, C. Suna and D. Xue, *Phys. Chem. Chem. Phys*., 2015, **17**, 732–750.

6 B. Lanson, Layered mineral structures and their application in advanced technologies, ed. M. F. Brigatti and A. Mottana, Mineralogical Society Great Britain & Ireland, London, 2011, pp. 151–202

7 S. Devaraj and N. Munichandraiah, *J. Phys. Chem. C.,* 2008, **112**, 4406–4417.

8 T. Brousse, M. Toupin, R. Dugas, L. Athouël, O. Crosnier and D. Bélanger, *J. Electrochem. Soc*., 2006, **153**, A2171–A2180.

9 H. Ohshima, Electrical Phenomena at Interfaces and Biointerfaces: Fundamentals and Applications in Nano-, Bio-, and Environmental Sciences, John Wiley & Sons, 2012, pp. 491–507.

10 K. Makgopa, P. M. Ejikeme, C. J. Jafta, K. Raju, M. Zeiger, V. Presser and K. I. Ozoemena, *J. Mater. Chem. A*, 2015, **3**, 3480-3490.

11 S. Devaraj and N. Munichandraiah, *J. Phys. Chem. C,* 2008, **112**, 4406–4417.

12 Z. Liu, K. Xu, H. Sun and S. Yin, *Small*, 2015, **11**, 2182–2191.

13 Y. Sun, L. Wang, Y. Liu and Y. Ren, *Small,* 2015, **11**, 300–305.

14 Y. Omomo, T. Sasaki, Lianzhou and M. Watanabe, *J. Am. Chem. Soc.,* 2003, **125**, 3568–3575.

15 G. Zhao, J. Li, L. Jiang, H. Dong, X. Wang and W. Hu, *Chem. Sci.*, 2012, **3**, 433–437.

16 N. Saito, J. Hieda and O. Takai, *Thin Solid Films*, 2009, **518**, 912–917.

17 A. Watthanaphanit and N. Saito, *Polym. Degrad. Stab*., 2013, **98**, 1072–1080.

18 J. Kang, O. L. Li, N. Saito, *Carbon*, 2013, **60**, 292–298.

19 O. L. Li, N. Takeuchi, Z. He, Y. Guo, K. Yasuoka, J. S. Chang and N. Saito, *Plasma. Chem. Plasma. P.*, 2012, **32**, 343–358.

20 O. Takai, *Pure Appl. Chem.,* 2008, **9**, 2003–2011.

21 J. Kang, O. L. Li and N. Saito, *Nanoscale*, 2013, **5**, 6874–6882.

22 A. Watthanaphanit, Y. K. Heo and N. Saito, *J. Taiwan Inst. Chem. Eng.,* 2014, **45**, 3099–3103.

23 Z. Liu, K. Xu, H. Sun, and S. Yin, *Small*, 2015, **11**, 2182–2191.

24 T. Fujimoto, Y. Mizukoshi, Y. Nagata, Y. Maeda and R. Oshima, *Scripta Mater*., 2001, **44**, 2183–2186.

25 A. Abulizi, G. H. Yang and K. Okitsu, *Ultrason. Sonochem.*, 2014, **21**, 1629–1634.

26 D. R. Bhumkar, H. M. Joshi, M. Sastry and V. B. Pokharkar, *Pharm Res*., 2007, **24**, 1415–1426.

27 A. Watthanaphanit, G. Panomsuwan and N. Saito, *RSC Adv.,* 2014, **4**, 1622–1629.

28 J. Zhu, Q. Li, W. Bi, L. Bai, X. Zhang, J. Zhou and Y. Xie, *J. Mater. Chem. A.*, 2013, **1**, 8154–8159.

29 C. Ji, H. Ren and S. C. Yang, *RSC Adv.,* 2015, **5**, 21978–21987.

30 K. Makgopa, P. M. Ejikeme, C. J. Jafta, K. Raju, M. Zeiger, V. Presser and K. I. Ozoemena, *J. Mater. Chem. A,* 2015, **3**, 3480-3490.

31 D. P. Dubal, D. S. Dhawale, R. R. Salunkhe and. C. D. Lokhande, *J. Electrochem. Soc.,* 2010, **157**, 812–817.

32 L. J. Sun and X.X. Liu, *European Polymer Journal*, 2008, **44**, 219–224.

33 C. Julien, M. Massot, R. Baddour-Hadjean, S. Franger, S. Bach, J. P. Pereira-Ramos, *Solid State Ionics*, 2003, **159**, 345–356.

34 C. M. Julien, M. Massot, and C. Poinsignon, *Spectrochim Acta A Mol Biomol Spectrosc.,* 2004, **60**, 689–700.

35 K. Kai, Y. Yoshida, H. Kageyama, G. Saito, T. Ishigaki, Y. Furukawa and J. Kawamata,

J. Am. Chem. Soc., 2008, **130**, 15938–15943.

36 S. S. Mujumdar, D. Curreli, S. G. Kapoor and D. Ruzic, *J. Manuf. Sci. Eng.*, 2014, **136**, 031011.

37 P. Pootawang, N. Saito and S. Y. Lee, *Nanotechnology,* 2013, **24**, 055604.

38 M. A. Bratescu, S. P. Cho, O. Takai and N Saito, *J. Phys. Chem. C*, 2011, **115**, 24569–24576.

39 K. Okitsu, M. Iwatani, B. Nanzai, R. Nishimura and Y. Maeda, *Ultrasonics Sonochemistry*, 2009, **16**, 387–391.